Article

Crystallographic texture and substructural phenomena in 316 stainless steel printed by selective laser melting

R. Santamaria[1], M. Salasi[1], W.D.A. Rickard[2], K. Pojtanabuntoeng[1], G. Leadbeater[1, 3], M. Iannuzzi[1], S.M. Reddy[4], M.Z. Quadir[1-3, *]

1 Curtin Corrosion Centre, Curtin University, Perth, WA, Australia; ricardo.santamar@postgrad.curtin.edu.au; mobin.salasi@curtin.edu.au; thunyaluk.pojtanabuntoeng@curtin.edu.au; mariano.iannuzzi@curtin.edu.au
2 Microscopy and Microanalysis Facility, John de Laeter Centre (JdLC), Perth, WA, Australia; w.rickard@curtin.edu.au
3 School of Civil and Mechanical Engineering, Perth, WA, Australia; g.leadbeater@exchange.curtin.edu.au
4 School of Earth and Planetary Sciences, Perth, WA, Australia; s.reddy@curtin.edu.au
* Correspondence: zakaria.quadir@curtin.edu.au; Tel.: +61(8) 08 9266 1026

Abstract: There is a fast-growing interest in the use of selective laser melting (SLM) for metal/alloy additive manufacturing. Our current knowledge of SLM printed 316 stainless steel (SS316) is limited and sometimes appears sporadic, presumably due to the complex interdependent effects of a large number of process variables of the SLM processing. This is reflected from the discrepant findings in the crystallographic textures and microstructures in this investigation with those reported in the literatures, which also vary itself. The as-printed material is macroscopically asymmetric in both the structures and crystallographic textures. The <101> and <111> crystallographic directions align parallel with the SLM scanning direction (SD) and build direction (BD), respectively. Likewise, some characteristic low angle boundary features are reported crystallographic, while this investigation unequivocally proves them non-crystallographic since they always maintain an identical alignment with the SLM laser scanning direction irrespective of the matrix material's crystal orientation. There is also 500±200 nm columnar or cellular features, depending on the cross-section, generally found all over the sample. These columnar or cellular features are formed with walls made of dense packing of dislocations entangled with Mn, Si and O enriched amorphous inclusions. They remain stable after the ASM solution treatments at 1050 °C temperatures, and therefore, are capable of hindering boundary migration events of recrystallization and grain growth. Thus, the nanoscale structures can be retained at high temperatures. Large 2-4 μm inclusions form during the solution treatment, within which the chemical and phase distribution are heterogeneous.

Keywords: Selective laser melting (SLM), 3D printing, Additive manufacturing (AM), 316 stainless steel (SS316), EBSD, TEM.

1. Introduction

The Selective laser melting (SLM) is a powder-based 3D printing/additive manufacturing (AM) technique for fabricating complex metallic parts with custom-designed internal and/or external structures. In SLM, a digital system drives a high power laser beam, up to 1 kW, along a predesigned track to melt and fuse metallic powder particles layer after layer to build a complex metal/alloy shape and/or internal structures that otherwise would be impossible to fabricate with conventional metal processing techniques. SLM was initially developed almost two decades ago [1], but until recently, it has been primarily used in laboratory-scale and industrial prototyping [2-5]. Over the last ten years, the manufacturing sector has shown a keen interest in using SLM for industrial mass production. This is primarily due to improvements in SLM printing hardware, e.g., laser precision, powder manufacturing, etc., to reduce time and production costs, as well as the increased regarding the inherent metallurgical benefits of SLM manufacturing [2-4]. SLM

 doi:10.20944/preprints202305.0537.v1

provides a high-degree of freedom in alloy compositions, covering both conventional and exotic mixtures, e.g., high entropy alloys, and provides a provision for post-heat treatments [6-8]. There are also unique metallurgical benefits for material light weighting and strengthening via the control of solidification rates and compositional gradients. These benefits are not possible, or highly restricted, in conventional metal casting and subsequent thermomechanical processing (TMP) [9-11]. As a result, the SLM technique is rapidly being incorporated into industrial manufacturing [12-14] particularly in the aerospace, automotive, biomedical and energy sectors [15-17].

The metallurgical process variables between conventional metal processing and SLM are significantly different [18,19]. Consequently, the materials properties, structures (at macro-, micro- and nano-scales), and application performance have large differences, even for the same alloy composition. Nevertheless, it should be noted that the majority of metal AM techniques are developed from the concept of conventional techniques such as casting, welding, powder processing and/or cladding. These conventional techniques are not ideal when developing additive manufacturing process parameters and variables, and Aboulkhair et al [18] have recently summarized the SLM process variables, and their differences with conventional processing. For instance, cast-ability and weld-ability are considered the primary characteristic for a given alloy's suitability for SLM fabrication. Indeed, there are marked differences between the solidification rates and conventional welding parameters and those involved in the SLM. Likewise, the re-melting and re-welding during subsequent SLM scanning creates a thermal effect that has some resemblances with the conventional TMP [5].

Our current SLM knowledge is limited to a handful alloy systems, including aluminum [19-22] and titanium [10,23,24] alloys, as well as some studies on stainless steel [25-28], nickel [29-32], cobalt [33-36], copper [37] and magnesium [38] alloys. Consistent and systematic investigations are essential to develop a detailed understanding of the effect of process variables on the microstructures and ultimate physical properties of SLM printed materials, as such, it has taken many decades of research to reach the current knowledge level for a given alloy system for a given conventional processing. The SLM journey has commenced, and the processes, microstructures and properties of materials processed in this way are in high demand because of the significant benefits and rapid growth of the technique. This paper presents a comprehensive analysis of the crystallography and composition of structures in an SLM printed 316 stainless steel (SS316) in the macro- to the nano-scales for advancing and rectifying our understanding on the structural and crystallographic texture phenomena.

2. Materials and Methods

SLM printing was conducted with a 3D system Pro X DMP 320 machine by a commercial 3D printing service company, Amiga Engineering. A SS316 powder feed supplied by TLS Technik GmbH & Co with 45±10 μm average size was used to print a rectangular block, see the schematic in Figure 1a inset. The other SLM parameters were 250W laser power, 250 mm/sec head speed and 30 μm scan resolution. The feed chemical composition was provided by the supplier as 0.02 wt.% C, 0.51 wt.% Si, 1.0 wt.% Mn. 17.5 wt.% Cr, 2.3 wt.% Mo, 11.1 wt.% Ni, and Fe balance.

The printed material was subjected to an isothermal solution treatment at 1050 °C for 4 hours in an argon-purged furnace followed by water quenching. The longitudinal cross-section ,see the schematic in Figure 1a inset, of both the as-printed and heat-treated samples were cut, mechanically polished down to colloidal silica finish, and then, ion milled with a Technoorg Linda SEMPrep II system to obtain a defect-free surface suitable for investigation by electron backscattered diffraction (EBSD) investigation. The ion milling parameters were 8 kV, 6° tilt and 360° rotation. EBSD was conducted with an Oxford Instruments Symmetry™ system attached to a Tescan Mira field emission scanning electron microscope (FE SEM) operated at 15 kV beam energy. Iron FCC (face centred cubic) phase

 doi:10.20944/preprints202305.0537.v1

from the Oxford database was used for indexing EBSD patterns and the Oxford Instruments' Channel 5 software was used to post-process and analyse the EBSD data.

Site-specific transmission electron microscopy (TEM) samples were prepared from bulk samples using a Tescan Lyra Ga^+ focused ion beam (FIB)-SEM. The final polishing step was done with low beam energy of 2 kV to minimize ion beam damage. A FEI Talos FS200X G2 FE TEM was use for the TEM investigation and was operated at 200 kV. Elemental mapping was conducted by an energy dispersive spectroscopy (EDS) attached as two pairs of a FEI Super X detection system. Location-specific diffraction analysis was performed using selective area diffraction (SAD) with a 200 nm diameter size aperture and convergent beam electron diffraction (CBED). A double tilt holder was used for tilting the sample to the intended crystallographic zone axis by navigating through the CBED generated Kikuchi pattern. TEM imaging was conducted both in conventional and scanning TEM (STEM) modes. For STEM, the bright field (BF) and high angle annular dark-field (HAADF) mode were used to enhance diffraction and atomic number contrast, respectively. TEM data acquisition and analysis was undertaken using Velox software and diffraction data analysis was conducted using the ICDD database.

3. Results and Discussion

3.1 Structural symmetry and crystallographic texture

Figures 1a-b show EBSD color coded inverse pole Figure (IPF) maps in the building direction (BD) and scanning direction (SD) in a BD-SD cross-section from a SLM printed block. The investigated cross-section schematic is shown in the inset in Figure 1a, in which the terminology of the orthogonal print axes is shown, in convention with comparable studies, e.g., [39]. In Figure 1, the optical micrograph shows the characteristic print features in an SD-TD surface previously reported in numerous investigations [39-42]. From the IPF maps, it is clear that the BD and SD were predominantly oriented along the <111> and <101> crystal directions, respectively. It is well-established that crystallographic texture in iron controls its anisotropy in mechanical, thermal, magnetic and optical properties. The observed macroscopic crystallographic texture is therefore likely to play a fundamental control on the anisotropy of physical properties in SLM printed SS316. The thick and thin black lines in the EBSD map represent the high-angle (>15°) and low-angle (3-15°) misorientation boundaries, respectively. The high-angle boundaries are broadly parallel to the laser scanning tracks associated with printing. There was no evidence of the formation of Σ9 twin boundary (<111>60°) in the as-printed sample. This finding is consistent with the other literature where no twin boundaries were reported in SLM printed SS316, although the wrought form of the material contains annealing twins [41,42].

In Figure 1b IPF map, there are thin <001> oriented layers, colored in red, between thicker <101> oriented printing tracks, colored in green. These green and red layers are called 'major-' and 'minor-layers' by Sun et al [43](pp. 89-93). The thickness of the major and minor layers varied between 100-200 μm and 50-100 μm, respectively, suggesting an overall crystallographic relationship between the major and minor layers. In both IPF maps, there are other orientations in the major layers, which are present in red and green regions in Figure 1a, and red and blue regions in Figure 1b. EBSD analysis in the TD revealed mixed orientation, not presented in the Figure. These findings suggest that a sample scale macroscopic crystallographic texture forms in SLM printed SS316, which is overall consistent with recent literature, but the reported textures vary in terms of crystal orientation [43-46]. An epitaxial growth mechanism between the major and minor layers is regarded as the origin of the overall texture development [43]. However, lattice epitaxy requires a perfect match between two lattice interfaces with common coincident sites, which is somewhat unrealistic to imagine in the SLM printed material, because it contains a continuous change of orientations, reflected by a gradual change in color, within short distances in the EBSD maps. Hence, a separate in-depth investigation at a finer length scale is required to find out if there are epitaxies over a short distance, and if that collectively develops the overall texture.

Preprints (www.preprints.org) | NOT PEER-REVIEWED | Posted: 8 May 2023 doi:10.20944/preprints202305.0537.v1

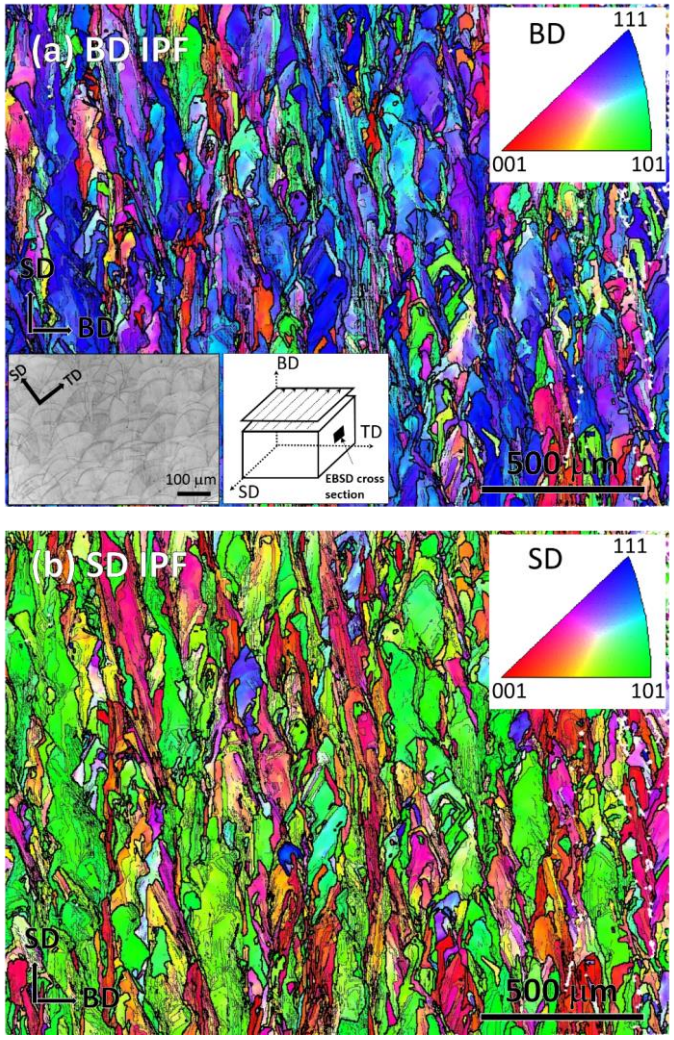

Figure 1. EBSD measured color-coded IPF map of the as printed SLM sample showing the orientation along the (a) BD and (b) SD. The insets in Figure 1a show the optical microscopy image and the EBSD cross-section.

In Figure 2a, the misorientation boundaries are elucidated in a higher resolution, 100 nm step size, IPF map, whereby the SD is plotted as per the color-coded IPF section in the inset. As before, the high- (>15°) and low-angle (3-15°) boundaries are represented by thick and thin black lines, respectively. The corresponding Kernel average misorientation (KAM) map is shown in Figure 2b, in which each data point represents the mean orientation difference with the eight surrounding neighboring points. The blue-yellow-red legend in Figure 2b indicates the relative KAM intensity. There was a correlation between Figure 2a and b viz. a comparison between the white encircled areas showing that the high stored energy spots have a higher density of misorientation boundaries. This observation can be understood in relation to dislocation density because a higher dislocation density is required to accommodate any misorientation. There were also regions of low stored energy. One such example is encompassed with a white rectangular box, within which there was a small orientation variation represented by a minor change in the IPF color variation. Such low misorientation variation indicates the presence of dislocation mesh and cell structures, which usually accommodate relatively less energy [47]. Therefore, the as-printed sample showed an overall heterogeneous distribution of the stored energy. This finding explains the spatial variation of the micro- and nano-scale mechanical data in the SLM printed material [48,49].

Figure 2a also reveals several other boundary morphological features. For example, the majority of the boundaries were straight, though there were a number of high-angle

Preprints (www.preprints.org) | NOT PEER-REVIEWED | Posted: 8 May 2023 doi:10.20944/preprints202305.0537.v1

boundaries that had convoluted trajectories, some of which are indicated with white arrows. Such a phenomenon indicates the occurrence of a thermally-induced restoration process, perhaps from the heat flow from the subsequent SLM scanning [47]. There was no sign of recrystallization, as noted by an absence of a trailed region with a uniform orientation behind a migrating high angle boundary [47]. The convoluted high-angle boundaries are expected to form during solidification or due to subsequent thermal restoration [47], though the process did not progress to the boundary migration stage of recrystallization.

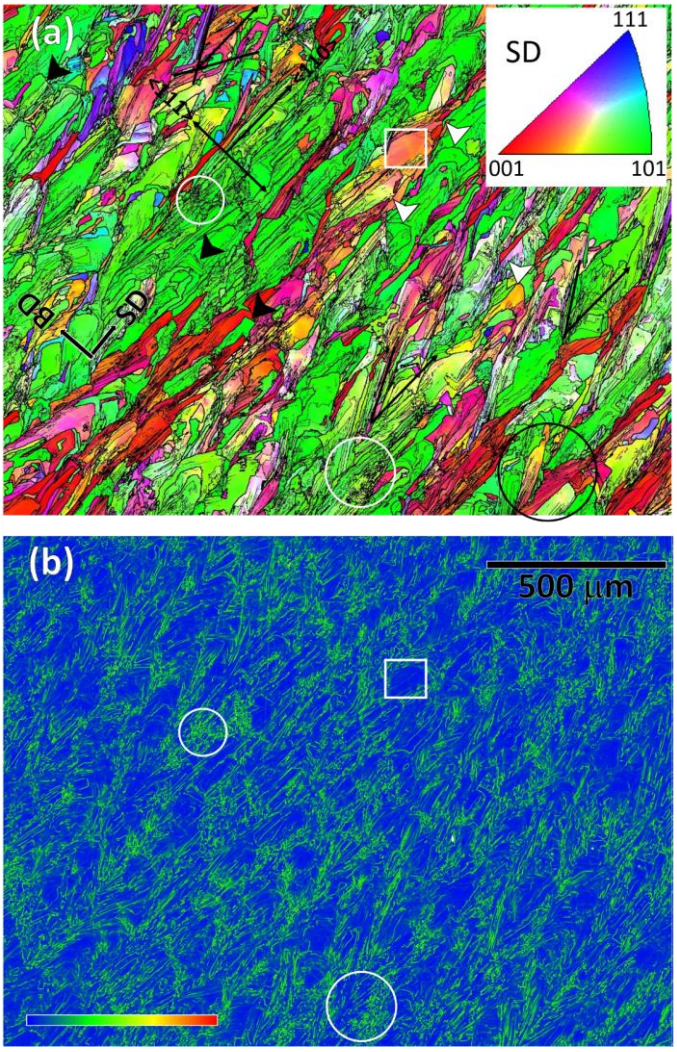

Figure 2. Higher resolution EBSD maps of the as printed SLM sample showing (a) color coded IPF map of SD to illustrate the inhomogeneities in the high (>15°) and low angle (3-15°) boundary distributions and their alignments with the SD and (b) the corresponding inhomogeneities in the KAM plot.

3.2 Substructural features

There is a profuse presence of straight misorientation boundaries in Figure 2a, aligned within a range of angles with the SD as indicated with black lines. Some straight boundaries are aligned along the SD, as given in Figure 2a, which is the <101> of the lattice direction. A small fraction also aligns at the right angle, in short segments pointed with the black arrows, which is along the BD || <111>. The remaining, which is the largest fraction of the straight boundaries, are aligned in the ±30-45° angular range, with the highest frequency at around ±35°. Some boundary combinations also resemble a leaf vein structure, with changing directions, one such example is encircled black in the right bottom in Figure 2a. Therefore, the overall alignment of the straight boundaries is rather complex,

 doi:10.20944/preprints202305.0537.v1

which Dinda et al [50](pp. 2152-2160) described as a function of the laser scanning strategy. In some recent studies, the boundaries appeared to have a coincidence with the crystallographic planes, most commonly along the {100} plane trace, e.g., SS316-, Ni-25% (Mo, Nb and Ti)-, Al-, Ta-, Ti-Mo-Zr-Al- and Mo-Si-alloys [43,44,50-55]. A few mechanisms for formation of these textures are outlined in the published literature based on the solid/liquid interface formation to explain their crystallographic origin. The scan rate and laser energy are reported to play a vital role in this regard [56]. In this investigation, however, the alignment of the straight boundaries remained invariably identical within an angular range with the SD, irrespective of the matrix orientation, as given in Figure 2a. For instance, the boundary orientations in the blue, located in the upper left, and red oriented regions comprise the same angular alignments with SD as the boundaries found the vast majority green regions. This suggests the low-angle straight boundaries are non-crystallographic viz. they do not preferentially form on a particular lattice plane trace(s). Although this conclusion is made based on unequivocal evidence, it should be noted that only a 3D EBSD could reveal the real crystallography of a 3D interface. There is evidence that 2D trace analysis of 3D boundary features may lead to misleading conclusions. One such example is the low angle microband boundaries that form in high stacking fault energy materials which were claimed both crystallographic [57] and non-crystallographic [58]. The debate continued until a reconciliation was achieved by a 3D EBSD investigation [59,60].

A recent article by Pham et al [46](p.749) accounts for the variations of boundary formation in SLM printed SS316, as that seen in Figure 2a. The fundamental basis remains identical to the previous reports, viz. the boundaries form along the solid-liquid interface during the solidification process [43,61,62]. In Pham et al's simulation work, it was demonstrated that side branching occurs, similarly to the current findings shown in Figures 1 and 2, during the solidification process, and thus alters the shape of the solidifying boundary front. As a result, the alignment of the solidification interface changes, and therefore, the formation of low-angle boundaries takes place over a wider angular range. The magnitude of side branching depends on a number of factors, primarily on the thermal gradient and heat flux, and the SLM parameters that control these two. Each narrative in the literatures on the low-angle crystallographic boundary formation, including Pham et al's study, are overwhelmed by the assumption that the solid/liquid interface appear as the crystallographic lattice interface. However, the physical details on the mechanism to explain how the habit plane or rotation axis correlate with a preferred crystal plane or direction are missing. Therefore, the mechanism of the low angle boundary formation is rather complicated because of the simultaneous occurrence of rapid solidification with the complex mechanical interaction of the semi-solid pool by the laser beam movement. In addition, there is a thermal pulsing during subsequent overlay of layers.

Numerous investigations have reported columnar structures that also appear as fine cellular structures in the transverse cross-section of the structure in the SLM printed SS316 [40,63,64]. An example of the cell structure is shown in a SEM image in the inset of Figure 3a. Unlike the low- and high-angle boundary structures in Figures 1 and 2, this structure was homogeneously found throughout the sample. Because of their submicron scale fineness, an electron transparent TEM sample was prepared by FIB-SEM site specific lift-out methods. Figure 3a shows a HAADF STEM image of the TEM sample whereby the columnar structures were sub-vertical in the cross-sectional lamellae. The walls of the columns are dense in dislocations and the walls are spaced parallel at 500 nm average distance. These boundaries were also decorated with 5-30 nm spherical particles. The particles were tangled within the boundary dislocations, see higher magnification image in Figure 3b, and created a pinning effect. These particles are likely to have restricted any thermally activated migration, and thus, retained the structures at a nanoscale. The dislocation walls were 50-150 nm in thickness and are expected to create a strain field, which became apparent by the diffraction contrast of the BF STEM imaging in Figure 3c, which was taken after tilting the sample so that the boundaries were edge-on. These dislocation features are expected to provide elevated strengthening in the SLM printed SS316 material

Preprints (www.preprints.org) | NOT PEER-REVIEWED | Posted: 8 May 2023 doi:10.20944/preprints202305.0537.v1

over the conventionally processed grade that usually comprises large equiaxed grains, hundreds of μm in size, and twin boundaries. This is reflected in a 20-50% improvement in the tensile strength in SLM printed SS316 over the conventional grade with identical chemical compositions [40]. The strength can also be improved by changing the laser strategy that works at a larger length scale. While further discussions on mechanical properties is outside the scope of the paper, it is expected from the results presented herein that superior strengthening at the micro- and nano-scale can be achieved in SLM printed grade due to the retention of nanostructures and formation of inclusions due to rapid cooling (~10^3–10^5 K/s) of SLM solidification [65].

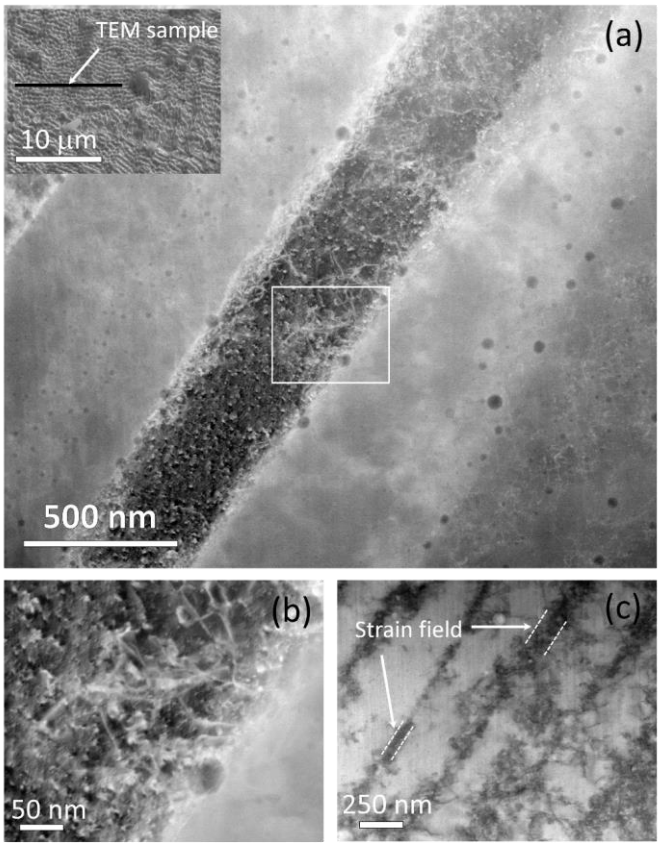

Figure 3. HAADF STEM images showing (a) particle decorations in dislocation constituted boundaries of the commonly found fine cell structures (in the inset) in SLM printed sample, and (b) particle pinning at the dislocation boundary in higher magnification HAADF STEM image of the rectangular area in Figures 3a, and (c) BF STEM image showing the strain field width of the dislocation boundaries at the boundaries edge on titled condition.

The darker appearance of the particles in the HAADF STEM images in Figure 3 indicates they had a lighter average atomic weight than the matrix. In Figure 4, an area was selected containing larger particles, which were used for elemental analysis by STEM-EDS. Elemental maps revealed that the particles were rich in Mn, Si and O. Significant effort was given to acquiring the crystallographic identity of the inclusions by using SAD and CBED diffraction techniques, but no diffraction spots were observed except those from the FCC iron matrix, and, therefore, these particles are likely amorphous. This finding is consistent with the report by Salman et al [64](pp. 205-212). It is pertinent to note, Shibata et al [66] (pp. 522-528) found larger particles, ~1 μm, with identical morphology in cast SS316. Those were characterized as MnO–SiO_2 particles, solely based on the chemical ratio measured by electron probe microanalysis and thermodynamic calculations. In some cases, they also found a small association of Cr_2O_3. In regard to the current study, it is important to note that Cr was not measured within the particle and no Cr-C crystalline

Preprints (www.preprints.org) | NOT PEER-REVIEWED | Posted: 8 May 2023 doi:10.20944/preprints202305.0537.v1

diffraction patterns were observed. Therefore, Cr is expected to remain in the solid solution to provide the intended stainless property in the SLM printed SS316.

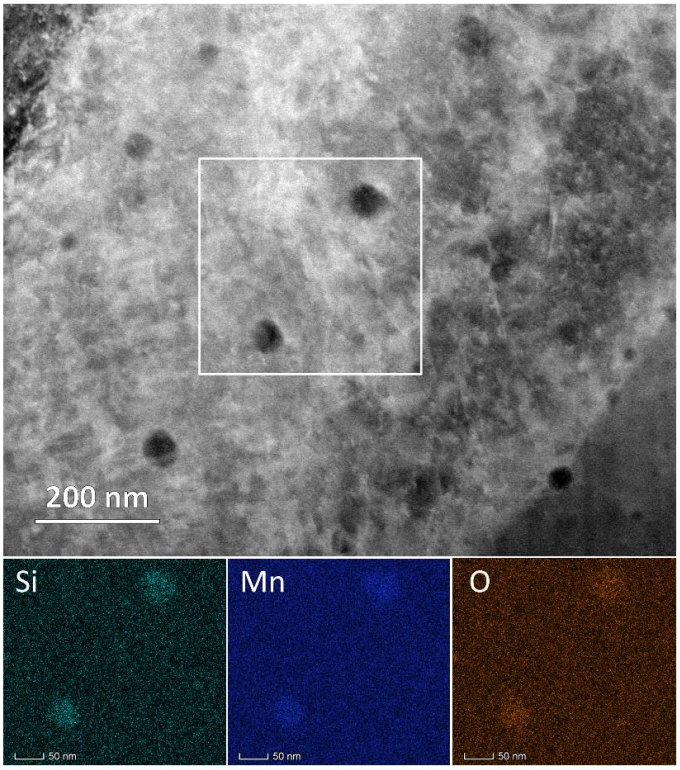

Figure 4. HAADF STEM image of the nano-particles and corresponding EDS measured elemental maps showing the particles are rich in Si, Mn and O content in the as pointed SLM sample.

3.3 Solution treatment structures

A solution treatment at 1050 °C for 4 h, per ASM [67] recommendations, of the as printed sample is expected to anneal any thermally unstable microstructures, and to ensure an uniform Cr dissolution into the matrix. It is pertinent to note the stainless properties get impaired in conventional grade SS316 because of the inadequate presence of atomic Cr in the solution that occurs due to Cr-C formation. The solution treatment brings the Cr atoms back to the matrix as solutes. Cr-containing inclusions were not observed in the samples in this study, see Figures 3 and 4, which suggests that the solution treatment is not needed for Cr dissolution purposes in the SLM material. However, the heterogeneous boundary structures shown in Figure 2, may result in an uneven Cr distribution because dislocations are naturally preferable sites for solute atoms. Therefore, the solution treatment may indeed promote an even Cr concentration.

Interestingly, only a subtle change took place in the substructures during the 1050 °C solution treatment. Figures 5a and b show a comparative view in the form of KAM maps that revealed an overall reduction in the KAM intensive boundary density after the solution treatment. The solution-treated structure is also shown in the BF STEM micrograph in Figure 5c, in which the dislocation constituted boundaries underwent a thermal relaxation process, compare with Figure 3, viz. the boundaries curved and dislocations were dissociated. The rectangular area in Figure 5c is magnified in the HAADF STEM image in Figure 5d. The analysis revealed boundary pinning by the inclusions that were found in the as-printed sample in Figures 3 and 4. They were measured to contain Mn, Si and O as per the as-printed sample. Overall, the inclusion density was significantly reduced by the solution treatment, perhaps because of some degree of dissolution and/or agglomeration. The high stability of the inclusions after the solution treatment at 1050 °C explains why recrystallization and grain growth did not take place in the SLM printed material. Earlier, Shibata et al [66] (pp. 522-528) reported that Mn-Si-O amorphous particles remain stable

 doi:10.20944/preprints202305.0537.v1

even after 1200 °C solution treatment in cast SS316, in which the grain growth was not prevented because the density was low and the inclusions size was large, >1 μm.

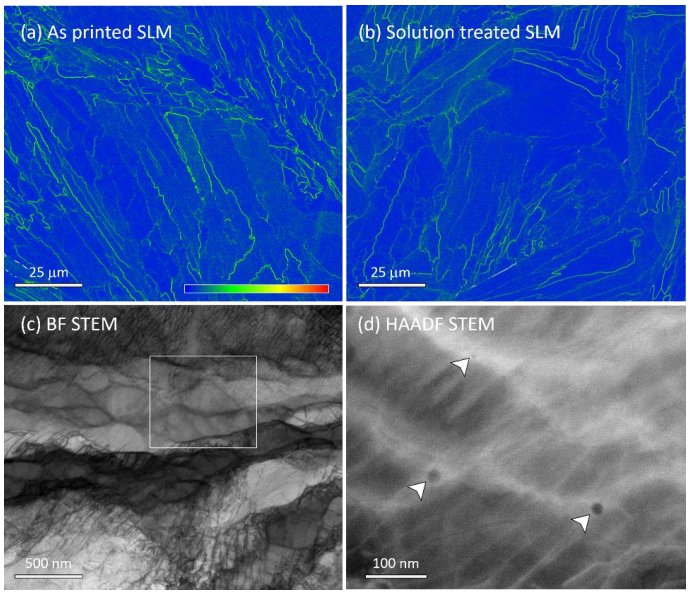

Figure 5. EBSD measured high-resolution KAM map showing the differences in the stored energy distributions between the (a) as printed and (b) solution treated SLM samples in the BD-SD cross-section. TEM investigation of the solution treated sample shows (c) the changes in the dislocation boundary structures in a BF STEM image and (d) the retention of boundaries by particle pinning in a magnified HAADF STEM image of the rectangular area marked in Figure c.

It is important to note that 2-4 μm large inclusions were also observed in the solution treated sample that were absent in the as-printed condition. An example is shown in the upper inset in Figure 6a, whereby a TEM lamella was prepared by FIB and presented in a STEM HAADF image (Figure 6a) to find the chemical distribution within the inclusion. The surrounding iron matrix appears brighter. It should be noted the TEM-EDS identified the inclusions were rich in Mn, Si, O though there was also Cr and O rich regions within the inclusion, also seen as brighter regions, as indicated by arrows, in the darker overall matrix. A SAD pattern from the marked area was taken and indexed as Cr_3O_4, as illustrated in the lower inset of Figure 6a. The iron matrix contained Cr as well, which is expected as solute. These findings suggest that during the solution treatment, a large fraction of the nano inclusions agglomerate into large 2-4 μm inclusions. The Cr from the solid solution also diffuses to participate in the inclusion formation, since Cr was not found in the inclusions in the as-printed sample. Overall, such large inclusions with a heterogeneous chemical and structural distribution can make the material more susceptible to corrosion. The effect is investigated by a dedicated corrosion study, and is currently under review as a separate manuscript. Therefore, the solution treatment recommended by ASM [67] for conventional SS316 is, indeed, expected to be detrimental for the SLM printed material.

Preprints (www.preprints.org) | NOT PEER-REVIEWED | Posted: 8 May 2023 doi:10.20944/preprints202305.0537.v1

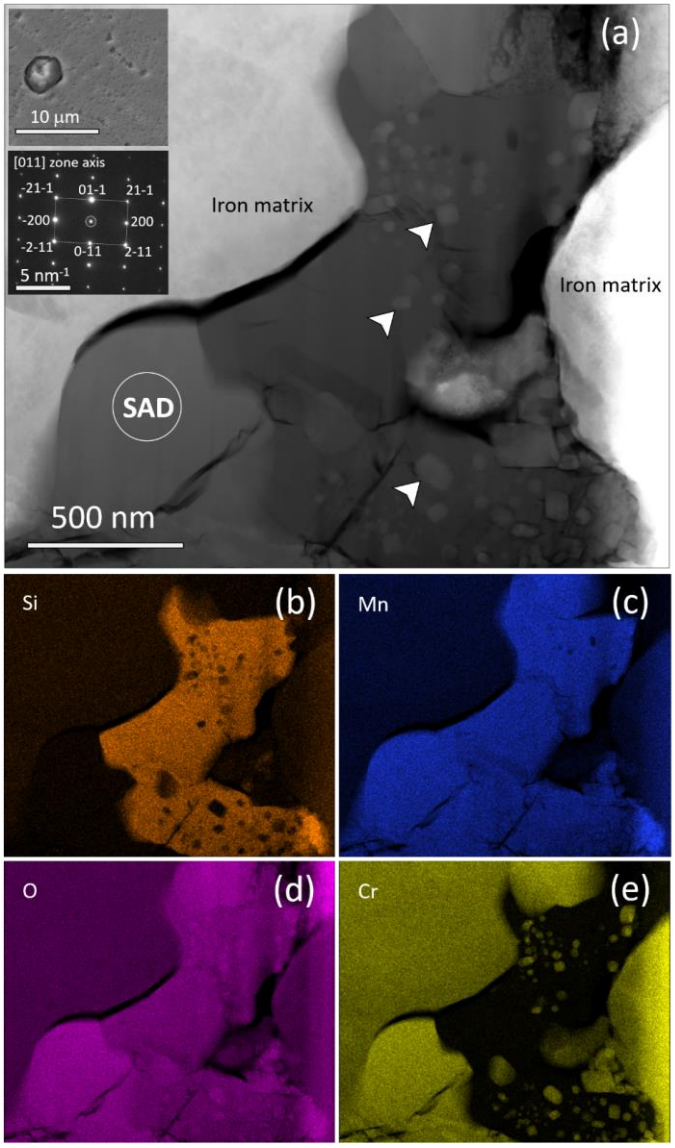

Figure 6. The structural and chemical heterogeneity of inclusion in the solution treated SLM printed sample is shown in (a) HAADF STEM image and (Figures b–d) corresponding elemental mapping. The insets in Figure a show, the inclusion from where the TEM sample was prepared, and the indexed SAD pattern of Cr_3O_4 from the SAD labelled area.

4. Conclusions

In this investigation, a thorough microscopy characterization of SLM SS316s/s in the as-printed and solution-annealed conditions was conducted at the macro-, micro- and nano-scales. The findings suggest some of the existing findings are inconclusive or imprecise, and require further investigation to mature our knowledge in this topic. The study summarizes the following conclusions:

1. SLM printed material possess asymmetric crystallographic texture and material structure. The microstructures have a distinctive structural morphology along the sample orthogonal axes and develops crystallographic textures of SD || <101> and BD || <111>.
2. A heterogeneous distribution of misorientation boundaries and stored energy were found throughout the SLM printed structures. Twin boundary formation was not observed in either the as-printed or solution-annealed samples.
3. In the as-printed structures, the typical straight misorientation boundaries were characterized as non-crystallographic. The boundaries maintained general alignments

with the SD within an angular range, irrespective of the matrix's crystal orientation, although there were occasional coincidences with crystal plane traces.

4. The high angle boundaries in the SLM substructures underwent thermal restoration, which were activated by the heat source from the subsequent layer printing. Pinning by the nano inclusions hindered classical recrystallization, and thus, prevented the formation of a defect-free annealing structure, even after 4 hours of solution treatment at 1050 °C.
5. A nano-scale lamellar structure, of 500±200 nm width, homogeneously formed throughout the printed material. Depending on the orientation, the structures appeared in cell or columnar morphologies in SEM and TEM images. Their boundaries contained dense dislocation structures tangled with fine amorphous inclusions containing Mn, Si and O. Cr was not detected in the inclusions above the detection limit. Hence, Cr remains in the matrix to provide the stainless properties.
6. Some degree of dissociation of the dislocation boundaries occurred during the solution treatment, but the overall refined structures are retained. Additionally, 2-4 μm large inclusions formed, comprising of composite structures and chemical distributions. These inclusions had detrimental characteristics for stainless performance.

Author Contributions: Conceptualization, R.S., M.Q., M.S., W.R., K.P., and S.R.; methodology, M.Q., M.S., W.R., K.P., and M.I.; validation, M.Q., W.R. and S.R.; formal analysis, R.S., M.S., and M.Q.; investigation, R.S., and M.Q.; resources, M.Q.; data curation, R.S., and M.Q..; writing—original draft preparation, R.S., and M.Q.; writing—review and editing, M.S., G.L., M.I., and S.R., ; visualization, R.S., W.R. and M.Q.; supervision, M.Q.; All authors have read and agreed to the published version of the manuscript.

Funding: This research received no external funding.

Institutional Review Board Statement: Not applicable.

Informed Consent Statement: Not applicable.

Data Availability Statement: This article contains all the data that was generated and is presented in the form of Figures.

Acknowledgments: The advanced characterization facility at Curtin's centralized research infrastructure hub, John de Laeter Centre (JdLC) is acknowledged for providing access to SEM, EBSD, TEM, FIB and sample preparation tools.

Conflicts of Interest: The authors declare no conflict of interest.

References

1. Meiners W, Wissenbach K, Gasser A (1998) Shaped body especially prototype or replacement part production. DE Patent 19

2. DebRoy T, Wei HL, Zuback JS, Mukherjee T, Elmer JW, Milewski JO, Beese AM, Wilson-Heid A, De A, Zhang W (2018) Additive manufacturing of metallic components – Process, structure and properties. Progress in Materials Science 92:112-224. doi:https://doi.org/10.1016/j.pmatsci.2017.10.001

3. Harun W, Kamariah M, Muhamad N, Ghani S, Ahmad F, Mohamed Z (2018) A review of powder additive manufacturing processes for metallic biomaterials. Powder Technology 327:128-151. doi:https://doi.org/10.1016/j.powtec.2017.12.058

4. Song B, Dong S, Deng S, Liao H, Coddet C (2014) Microstructure and tensile properties of iron parts fabricated by selective laser melting. Optics & Laser Technology 56:451-460. doi:https://doi.org/10.1016/j.optlastec.2013.09.017

5. Olakanmi EO, Cochrane RF, Dalgarno KW (2015) A review on selective laser sintering/melting (SLS/SLM) of aluminium alloy powders: Processing, microstructure, and properties. Progress in Materials Science 74:401-477. doi:https://doi.org/10.1016/j.pmatsci.2015.03.002

6. Liu Z, Zhang D, Sing S, Chua C, Loh L (2014) Interfacial characterization of SLM parts in multi-material processing: Metallurgical diffusion between 316L stainless steel and C18400 copper alloy. Materials Characterization 94:116-125. doi:https://doi.org/10.1016/j.matchar.2014.05.001

7. Shi R, Khairallah SA, Roehling TT, Heo TW, McKeown JT, Matthews MJ (2020) Microstructural control in metal laser powder bed fusion additive manufacturing using laser beam shaping strategy. Acta Materialia 184:284-305. doi:https://doi.org/10.1016/j.actamat.2019.11.053

8. Mower TM, Long MJ (2016) Mechanical behavior of additive manufactured, powder-bed laser-fused materials. Materials Science and Engineering: A 651:198-213. doi:https://doi.org/10.1016/j.msea.2015.10.068

9. Maconachie T, Leary M, Lozanovski B, Zhang X, Qian M, Faruque O, Brandt M (2019) SLM lattice structures: Properties, performance, applications and challenges. Materials & Design 183:108137. doi:https://doi.org/10.1016/j.matdes.2019.108137

10. Maskery I, Aremu A, Simonelli M, Tuck C, Wildman R, Ashcroft I, Hague R (2015) Mechanical properties of Ti-6Al-4V selectively laser melted parts with body-centred-cubic lattices of varying cell size. Experimental Mechanics 55:1261-1272. doi:https://doi.org/10.1007/s11340-015-0021-5

11. Maskery I, Aboulkhair N, Aremu A, Tuck C, Ashcroft I, Wildman RD, Hague R (2016) A mechanical property evaluation of graded density Al-Si10-Mg lattice structures manufactured by selective laser melting. Materials Science and Engineering: A 670:264-274. doi:https://doi.org/10.1016/j.msea.2016.06.013

12. Hamilton RF, Bimber BA, Andani MT, Elahinia M (2017) Multi-scale shape memory effect recovery in NiTi alloys additive manufactured by selective laser melting and laser directed energy deposition. Journal of Materials Processing Technology 250:55-64. doi:https://doi.org/10.1016/j.jmatprotec.2017.06.027

13. Visser CW, Pohl R, Sun C, Römer GW, Huis in ‘t Veld B, Lohse D (2015) Toward 3D printing of pure metals by laser‐induced forward transfer. Advanced materials 27 (27):4087-4092. doi:https://doi.org/10.1002/adma.201501058

14. Li Y, Gu D (2014) Parametric analysis of thermal behavior during selective laser melting additive manufacturing of aluminum alloy powder. Materials & design 63:856-867. doi:https://doi.org/10.1016/j.matdes.2014.07.006

15. Averyanova M, Cicala E, Bertrand P, Grevey D (2012) Experimental design approach to optimize selective laser melting of martensitic 17‐4 PH powder: part I‐single laser tracks and first layer. Rapid Prototyping Journal. doi:https://doi.org/10.1108/13552541211193476

16. Lott P, Schleifenbaum H, Meiners W, Wissenbach K, Hinke C, Bültmann J (2011) Design of an optical system for the in situ process monitoring of selective laser melting (SLM). Physics Procedia 12:683-690. doi:https://doi.org/10.1016/j.phpro.2011.03.085

17. Brecher C (2015) Advances in production technology. Springer Nature,

18. Aboulkhair NT, Simonelli M, Parry L, Ashcroft I, Tuck C, Hague R (2019) 3D printing of Aluminium alloys: Additive Manufacturing of Aluminium alloys using selective laser melting. Progress in materials science 106:100578. doi:https://doi.org/10.1016/j.pmatsci.2019.100578

19. Aboulkhair NT, Everitt NM, Ashcroft I, Tuck C (2014) Reducing porosity in AlSi10Mg parts processed by selective laser melting. Additive manufacturing 1:77-86. doi:https://doi.org/10.1016/j.addma.2014.08.001

20. Langelaar M (2016) Topology optimization of 3D self-supporting structures for additive manufacturing. Additive manufacturing 12:60-70. doi:https://doi.org/10.1016/j.addma.2016.06.010

21. Read N, Wang W, Essa K, Attallah MM (2015) Selective laser melting of AlSi10Mg alloy: Process optimisation and mechanical properties development. Materials & Design (1980-2015) 65:417-424. doi:https://doi.org/10.1016/j.matdes.2014.09.044

22. Aboulkhair NT, Everitt NM, Maskery I, Ashcroft I, Tuck C (2017) Selective laser melting of aluminum alloys. MRS Bulletin 42 (4):311-319. doi:https://doi.org/10.1557/mrs.2017.63

23. Simonelli M, Tse YY, Tuck C (2014) Effect of the build orientation on the mechanical properties and fracture modes of SLM Ti–6Al–4V. Materials Science and Engineering: A 616:1-11. doi:https://doi.org/10.1016/j.msea.2014.07.086

24. Simonelli M, Tse YY, Tuck C (2014) On the texture formation of selective laser melted Ti-6Al-4V. Metallurgical and Materials Transactions A 45:2863-2872. doi:https://doi.org/10.1007/s11661-014-2218-0

25. Kamath C, El-Dasher B, Gallegos GF, King WE, Sisto A (2014) Density of additively-manufactured, 316L SS parts using laser powder-bed fusion at powers up to 400 W. The International Journal of Advanced Manufacturing Technology 74:65-78. doi:https://doi.org/10.1007/s00170-014-5954-9

26. Garibaldi M, Ashcroft I, Lemke J, Simonelli M, Hague R (2018) Effect of annealing on the microstructure and magnetic properties of soft magnetic Fe-Si produced via laser additive manufacturing. Scripta Materialia 142:121-125. doi:https://doi.org/10.1016/j.scriptamat.2017.08.042

27. Garibaldi M, Ashcroft I, Simonelli M, Hague R (2016) Metallurgy of high-silicon steel parts produced using Selective Laser Melting. Acta Materialia 110:207-216. doi:https://doi.org/10.1016/j.actamat.2016.03.037

28. Lemke J, Simonelli M, Garibaldi M, Ashcroft I, Hague R, Vedani M, Wildman R, Tuck C (2017) Calorimetric study and microstructure analysis of the order-disorder phase transformation in silicon steel built by SLM. Journal of Alloys and Compounds 722:293-301. doi:https://doi.org/10.1016/j.jallcom.2017.06.085

29. Catchpole-Smith S, Aboulkhair N, Parry L, Tuck C, Ashcroft IA, Clare A (2017) Fractal scan strategies for selective laser melting of 'unweldable'nickel superalloys. Additive Manufacturing 15:113-122. doi:https://doi.org/10.1016/j.addma.2017.02.002

30. Choi J-P, Shin G-H, Yang S, Yang D-Y, Lee J-S, Brochu M, Yu J-H (2017) Densification and microstructural investigation of Inconel 718 parts fabricated by selective laser melting. Powder Technology 310:60-66. doi:https://doi.org/10.1016/j.powtec.2017.01.030

31. Marchese G, Garmendia Colera X, Calignano F, Lorusso M, Biamino S, Minetola P, Manfredi D (2017) Characterization and comparison of Inconel 625 processed by selective laser melting and laser metal deposition. Advanced Engineering Materials 19 (3):1600635. doi:https://doi.org/10.1002/adem.201600635

32. Carter LN, Martin C, Withers PJ, Attallah MM (2014) The influence of the laser scan strategy on grain structure and cracking behaviour in SLM powder-bed fabricated nickel superalloy. Journal of Alloys and Compounds 615:338-347. doi:https://doi.org/10.1016/j.jallcom.2014.06.172

33. Ciurana J, Hernandez L, Delgado J (2013) Energy density analysis on single tracks formed by selective laser melting with CoCrMo powder material. The International Journal of Advanced Manufacturing Technology 68:1103-1110. doi:https://doi.org/10.1007/s00170-013-4902-4

34. Pupo Y, Delgado J, Serenó L, Ciurana J (2013) Scanning space analysis in selective laser melting for CoCrMo powder. Procedia Engineering 63:370-378. doi:https://doi.org/10.1016/j.proeng.2013.08.228

35. Monroy K, Delgado J, Ciurana J (2013) Study of the pore formation on CoCrMo alloys by selective laser melting manufacturing process. Procedia Engineering 63:361-369. doi:https://doi.org/10.1016/j.proeng.2013.08.227

36. Takaichi A, Nakamoto T, Joko N, Nomura N, Tsutsumi Y, Migita S, Doi H, Kurosu S, Chiba A, Wakabayashi N (2013) Microstructures and mechanical properties of Co–29Cr–6Mo alloy fabricated by selective laser melting process for dental applications. Journal of the mechanical behavior of biomedical materials 21:67-76. doi:https://doi.org/10.1016/j.jmbbm.2013.01.021

37. Yadroitsev I, Gusarov A, Yadroitsava I, Smurov I (2010) Single track formation in selective laser melting of metal powders. Journal of Materials Processing Technology 210 (12):1624-1631. doi:https://doi.org/10.1016/j.jmatprotec.2010.05.010

38. Zhang B, Liao H, Coddet C (2012) Effects of processing parameters on properties of selective laser melting Mg–9% Al powder mixture. Materials & Design 34:753-758. doi:https://doi.org/10.1016/j.matdes.2011.06.061

39. Galy C, Le Guen E, Lacoste E, Arvieu C (2018) Main defects observed in aluminum alloy parts produced by SLM: From causes to consequences. Additive Manufacturing 22:165-175. doi:https://doi.org/10.1016/j.addma.2018.05.005

40. Suryawanshi J, Prashanth KG, Ramamurty U (2017) Mechanical behavior of selective laser melted 316L stainless steel. Materials Science and Engineering: A 696:113-121. doi:https://doi.org/10.1016/j.msea.2017.04.058

41. Michiuchi M, Kokawa H, Wang Z, Sato Y, Sakai K (2006) Twin-induced grain boundary engineering for 316 austenitic stainless steel. Acta materialia 54 (19):5179-5184. doi:https://doi.org/10.1016/j.actamat.2006.06.030

42. Godec M, Zaefferer S, Podgornik B, Šinko M, Tchernychova E (2020) Quantitative multiscale correlative microstructure analysis of additive manufacturing of stainless steel 316L processed by selective laser melting. Materials Characterization 160:110074. doi:https://doi.org/10.1016/j.matchar.2019.110074

43. Sun S-h, Ishimoto T, Hagihara K, Tsutsumi Y, Hanawa T, Nakano T (2019) Excellent mechanical and corrosion properties of austenitic stainless steel with a unique crystallographic lamellar microstructure via selective laser melting. Scripta Materialia 159:89-93. doi:https://doi.org/10.1016/j.scriptamat.2018.09.017

44. Sun S-H, Hagihara K, Nakano T (2018) Effect of scanning strategy on texture formation in Ni-25 at.% Mo alloys fabricated by selective laser melting. Materials & Design 140:307-316. doi:https://doi.org/10.1016/j.matdes.2017.11.060

45. Thijs L, Sistiaga MLM, Wauthle R, Xie Q, Kruth J-P, Van Humbeeck J (2013) Strong morphological and crystallographic texture and resulting yield strength anisotropy in selective laser melted tantalum. Acta Materialia 61 (12):4657-4668. doi:https://doi.org/10.1016/j.actamat.2013.04.036

46. Pham M-S, Dovgyy B, Hooper PA, Gourlay CM, Piglione A (2020) The role of side-branching in microstructure development in laser powder-bed fusion. Nature communications 11 (1):749. doi:https://doi.org/10.1038/s41467-020-14453-3

47. Humphreys F, Hatherly M (2004) Chapter 12-recrystallization textures. Recrystallization and Related Annealing Phenomena, second ed, Elsevier, Oxford:379e413

48. Prashanth K, Shahabi HS, Attar H, Srivastava V, Ellendt N, Uhlenwinkel V, Eckert J, Scudino S (2015) Production of high strength Al85Nd8Ni5Co2 alloy by selective laser melting. Additive Manufacturing 6:1-5. doi:https://doi.org/10.1016/j.addma.2015.01.001

49. Qi T, Zhu H, Zhang H, Yin J, Ke L, Zeng X (2017) Selective laser melting of Al7050 powder: Melting mode transition and comparison of the characteristics between the keyhole and conduction mode. Materials & Design 135:257-266. doi:https://doi.org/10.1016/j.matdes.2017.09.014

50. Dinda G, Dasgupta A, Mazumder J (2012) Evolution of microstructure in laser deposited Al–11.28% Si alloy. Surface and Coatings Technology 206 (8-9):2152-2160. doi:https://doi.org/10.1016/j.surfcoat.2011.09.051

51. Wei H, Mazumder J, DebRoy T (2015) Evolution of solidification texture during additive manufacturing. Scientific reports 5 (1):1-7. doi:https://doi.org/10.1038/srep16446

52. Bhattacharya S, Dinda GP, Dasgupta AK, Mazumder J (2014) A comparative study of microstructure and mechanical behavior of CO 2 and diode laser deposited Cu–38Ni alloy. Journal of Materials Science 49:2415-2429. doi:https://doi.org/10.1007/s10853-013-7883-7

53. Parimi LL, Ravi G, Clark D, Attallah MM (2014) Microstructural and texture development in direct laser fabricated IN718. Materials Characterization 89:102-111. doi:https://doi.org/10.1016/j.matchar.2013.12.012

54. Yadollahi A, Shamsaei N, Thompson SM, Seely DW (2015) Effects of process time interval and heat treatment on the mechanical and microstructural properties of direct laser deposited 316L stainless steel. Materials Science and Engineering: A 644:171-183. doi:https://doi.org/10.1016/j.msea.2015.07.056

55. Dinda G, Dasgupta A, Bhattacharya S, Natu H, Dutta B, Mazumder J (2013) Microstructural characterization of laser-deposited Al 4047 alloy. Metallurgical and Materials Transactions A 44:2233-2242. doi:https://doi.org/10.1007/s11661-012-1560-3

56. Ishimoto T, Hagihara K, Hisamoto K, Sun S-H, Nakano T (2017) Crystallographic texture control of beta-type Ti–15Mo–5Zr–3Al alloy by selective laser melting for the development of novel implants with a biocompatible low Young's modulus. Scripta Materialia 132:34-38. doi:https://doi.org/10.1016/j.scriptamat.2016.12.038

57. Winther G, Jensen DJ, Hansen N (1997) Dense dislocation walls and microbands aligned with slip planes—theoretical considerations. Acta materialia 45 (12):5059-5068. doi:https://doi.org/10.1016/S1359-6454(97)00168-7

58. Hurley P, Bate P, Humphreys F (2003) An objective study of substructural boundary alignment in aluminium. Acta Materialia 51 (16):4737-4750. doi:https://doi.org/10.1016/S1359-6454(03)00277-5

59. Afrin N, Quadir MZ, Xu W, Ferry M (2012) Spatial orientations and structural irregularities associated with the formation of microbands in a cold deformed Goss oriented Ni single crystal. Acta materialia 60 (18):6288-6300. doi:https://doi.org/10.1016/j.actamat.2012.08.003

60. Afrin N, Quadir MZ, Bassman L, Driver J, Albou A, Ferry M (2011) The three-dimensional nature of microbands in a channel die compressed Goss-oriented Ni single crystal. Scripta Materialia 64 (3):221-224. doi:https://doi.org/10.1016/j.scriptamat.2010.10.020

61. Wei H, Elmer J, DebRoy T (2016) Origin of grain orientation during solidification of an aluminum alloy. Acta Materialia 115:123-131. doi:https://doi.org/10.1016/j.actamat.2016.05.057

62. Wang Y, Shi J (2020) Developing very strong texture in a nickel-based superalloy by selective laser melting with an ultra-high power and flat-top laser beam. Materials Characterization 165:110372. doi:https://doi.org/10.1016/j.matchar.2020.110372

63. Wang YM, Voisin T, McKeown JT, Ye J, Calta NP, Li Z, Zeng Z, Zhang Y, Chen W, Roehling TT (2018) Additively manufactured hierarchical stainless steels with high strength and ductility. Nature materials 17 (1):63-71. doi:https://doi.org/10.1038/nmat5021

64. Salman O, Gammer C, Chaubey A, Eckert J, Scudino S (2019) Effect of heat treatment on microstructure and mechanical properties of 316L steel synthesized by selective laser melting. Materials Science and Engineering: A 748:205-212. doi:https://doi.org/10.1016/j.msea.2019.01.110

65. Huang C, Yan X, Zhao L, Liu M, Ma W, Wang W, Soete J, Simar A (2019) Ductilization of selective laser melted Ti6Al4V alloy by friction stir processing. Materials Science and Engineering: A 755:85-96. doi:https://doi.org/10.1016/j.msea.2019.03.133

66. Shibata H, Tanaka T, Kimura K, Kitamura S-Y (2010) Composition change in oxide inclusions of stainless steel by heat treatment. Ironmaking & Steelmaking 37 (7):522-528. doi:https://doi.org/10.1179/030192310X12700328925903

67. Dossett J, Totten G (2014) Heat Treating of Austenitic and Duplex Stainless Steels. doi:https://doi.org/10.31399/asm.hb.v04d.a0005990